

PARIS SACLAY

Master's Thesis in NanoScience

Design of an AlGaAs on-chip device to generate a OAM/SAM light beam

Author:
Giorgio Maltese

Supervisor:
Yacine Halioua

Advisor:
prof. Sara Ducci

July 9, 2015

Acknowledgments

I would like to express my deep gratitude to prof. Sara Ducci for giving me the opportunity to work in her group on a very interesting project. Her warm encouragement never let me down and her guidance helped me to stay focused even in hard times. I am also extremely thankful to the researcher Yacine Halioua for patiently sharing with me his experience and knowledge. Besides, he taught me how to approach complex problems, such as the design of a completely new device. I am grateful to the PhD Guillaume Boucher for teaching me how to present data in a professional manner and to the postdocs Pierre and Qui Feng for many inspiring discussions about physics. I also take this opportunity to express my gratitude to all the other members of DON team at MPQ for their incessant support and friendship. Thanks to them, I had a very good time during the whole stage. Finally, I would like to thank my classmates for the great year we spent together and to give special thanks to my girlfriend, all my friends and my family for their endless support.

1 Abstract

We propose an on-chip device based on aluminium gallium arsenide (AlGaAs) which allows to "spin" and "twist" a linearly polarized (LP) beam at the telecom wavelength ($\lambda = 1.55\mu\text{m}$). At the device output, the beam carries both spin angular momentum (SAM) and orbital angular momentum (OAM). The latter one is particularly interesting for coding quantum states on an unbounded basis, which could lead to faster and safer quantum communication protocols on chip. The AlGaAs platform, having a direct band gap, can be employed to fabricate active devices such as lasers, other than devices based on χ^2 non linear effects (e.g. Parametric Down Conversion) and electro-optic effects. This device is designed to be monomode, easy to fabricate and has low losses.

Contents

Acknowledgments	2
1 Abstract	3
2 Introduction	1
2.1 Context	1
2.2 AlGaAs integrated photon pairs sources	1
2.3 AlGaAs device to generate a light beam carrying OAM	2
3 Spin and Orbital Angular Momentum of light	4
3.1 Angular momentum of light	4
3.2 Spin Angular Momentum	5
3.3 Orbital Angular Momentum	6
3.3.1 HG to LG transformation	7
3.3.2 Generation of an OAM light beam in a waveguide	9
4 OAM/SAM light beam generated by a AlGaAs on-chip mode converter	11
4.1 AlGaAs based device	11
4.2 Design guidelines	11
4.2.1 OAM generation	12
4.2.2 Conversion efficiency	12
4.2.3 Fabrication tolerances	12
4.3 Device structure	13
4.3.1 Layers composition	14
4.3.2 Geometry	14
4.4 $\frac{\pi}{2}$ phase-shift by use of an asymmetric waveguide	15
4.5 OAM/SAM beam at the output of the device	18
5 Device optimization and tolerances study	20
5.1 Input Coupling	20
5.2 Monomode Condition	24
5.3 Delay	25
5.4 Losses	27
5.5 Diffraction	27
5.6 Growth tolerances	28
6 Conclusion and Perspectives	30
Bibliography	31

2 Introduction

2.1 Context

At the beginning of the previous century Albert Einstein unveiled the quantum nature of light by predicting its wave-particle duality. Sixty years later, the development of laser has allowed to produce coherent and monochromatic light beams, which could be manipulated through optical devices. Since then, optics has been the perfect choice for quantum information, the field that studies how information is encoded, manipulated and detected in quantum systems.

As instance, one important field of quantum information is quantum communication, whose protocols are much more secure than the corresponding classical ones. The most common is quantum key distribution (QKD), based on the impossibility to copy secret keys, encoded in quantum states, without corrupting them.

Nowadays our challenge is to take advantage of these new technologies in integrated quantum photonic devices, directly compatible with the existing telecom network and operating at room temperature. For such purpose, semiconductor materials like silicon (Si) and aluminum gallium arsenite (AlGaAs) are in pole position. The main advantage of Si is its compatibility with the CMOS technology, but its indirect band gap makes the fabrication of electrically driven sources difficult. Furthermore its lattice structure does not permit to generate photon pairs via non linear phenomena of the second order, so people need to rely on the third order non linear effects, which are smaller. An important example of second order non linear effect is spontaneous parametric down conversion (SPDC). In SPDC one incoming photons generates two photons who share its energy. During this process also the system total momentum must be conserved, as the phase-matching condition states. For SPDC AlGaAs material is more suitable: the symmetry of its lattice structure is compatible with second order non linear conversions, while its refractive index range $n \in [2.98, 3.37]$ is wide enough to allow a fine phase-matching engineering. Moreover, AlGaAs presents a direct band gap that allows a radiative recombination, hence lasers.

2.2 AlGaAs integrated photon pairs sources

AlGaAs integrated quantum sources, based on SPDC, have been demonstrated at the MPQ laboratory (Laboratoire Matériaux et Phénomènes Quantiques) by the DON team (Dispositifs Optiques Nonlinéaires), in Paris Diderot university.

Among them, we can mention an electrical pumped source of photons pairs [19], illustrated in fig. 2.1 (on the left), and a transversely optically pumped source of counter propagating twin photons, represented in fig. 2.1 (on the right), conceived to engineer the frequency state of the photon pairs with great versatility [26].

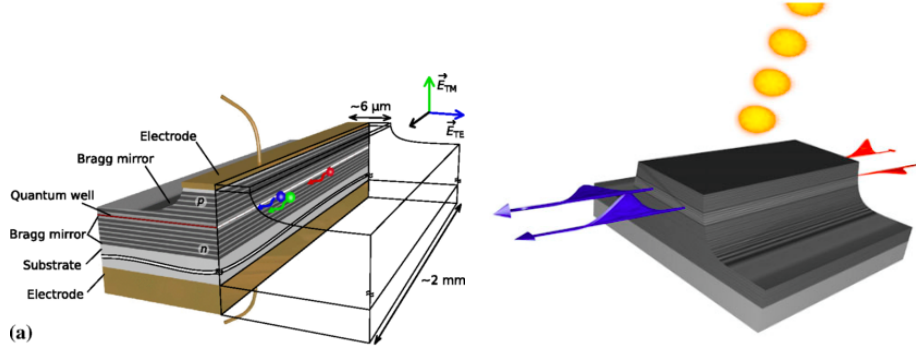


Figure 2.1: AlGaAs sources of twin photons developed at MPQ in DON team. On the left, the AlGaAs electrically pumped photons pairs source. The intra cavity SPDC is induced by photons generated in the electrically pumped quantum well. On the right, the AlGaAs optical pumped device. A pump beam impinges on top of the waveguide and produces one of two possible twin photons states. Phase-matching is satisfied automatically along the waveguide direction, while a periodic modulation of the waveguide core is required in the epitaxial direction.

2.3 AlGaAs device to generate a light beam carrying OAM

These devices have been conceived to generate quantum states in which photons are entangled in frequency and polarization. However, light offers an additional physical quantity to play with. As Allen showed in 1992 [2], light beams carry an orbital angular momentum (OAM), a degree of freedom that allows the generation of hyper-entangled quantum states [3].

In the past fifteen years, OAM light beams have been investigated in free space quantum optics and quantum communication experiments [23, 36]. These twisting beams are interesting because of their potential infinite number of states, in contrast to the only two orthogonal states offered by polarization. As qu-bits (0,1) can be encoded in the polarization state of photons [16], photons with OAM can be the carrier of qu-dits (a, b, c, d, e, \dots), a superposition of d different quantum states [11]. Since the unit of information is much richer, the number of channels for the propagating information increases while more complex secret keys can be used. As a result, faster and safer communications are possible.

Besides, OAM of light has found applications in many other fields as well, like particle micromanipulation [31], imaging [13], free space communication system [39] and even astronomy [37]. It has also contributed to pioneering fundamental physics, leading to the discovery of rotational Doppler frequency shift [9] other than the formalization of angular uncertainty relations [12] and Poincaré hyper-spheres [28].

Nowadays, one of the challenges of OAM optics is to generate and propagates OAM light beams in integrated chips. Some of the main difficulties in guiding OAM light beams in waveguides are the rotational symmetry requirements and the intermodal coupling. Still, starting from a recently published proposal on a SOI device [21], we de-

sign a monomode and ideally lossless device, based on AlGaAs, to generate a light beam carrying OAM. The main goal for the future is to start from this integrated device to generate hyper-entangled OAM quantum states. Since our device is based on AlGaAs, a miniature electrical pumped AlGaAs OAM laser could be designed and realized as well.

3 Spin and Orbital Angular Momentum of light

3.1 Angular momentum of light

In 1619 Kepler observed that comets' tail always points away from the Sun and explained it by introducing for the first time the concept of radiation pressure of light [18]. To explain light radiation pressure, in 1862 Maxwell introduced the idea of linear momentum of light and in 1900 Lebedev proved it experimentally [20]. Nowadays it is well known that light carries a linear momentum \mathbf{p} , directed along its direction of propagation \mathbf{k} and with an amplitude of $p = \frac{h}{\lambda}$ per photon, as states by the de Broglie's relation. It is less known that, in addition to \mathbf{p} , a light beam can also posses an angular momentum \mathbf{L} , directed along the direction of propagation of light as well. To visualise it, we may consider a light beam propagating along x and a particle situated in the transverse plane at the position \mathbf{r} from the beam axis (fig. 3.1).

If the beam carries an angular momentum, it would exert on the particle an impulse given by the classical definition $\mathbf{L} = \mathbf{r} \times \mathbf{p}$.

This relation can be satisfied by two different kind of light beams. The first one (fig. 3.1, on the left) is a circularly polarized beam and carries a spin angular momentum (SAM, $\mathbf{L} = \mathbf{L}_s$), which makes the particle spins around its axis. The other one (fig. 3.1, on the right), has a helicoidal phase structure and carries orbital angular momentum (OAM, $\mathbf{L} = \mathbf{L}_o$), which forces the particle to rotate in a circular orbit, following the beam phase structure.

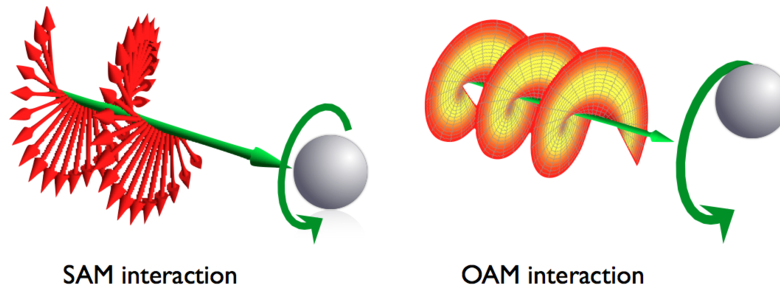


Figure 3.1: Comparison between SAM (left) and OAM (right) light beams, as they interact with a particle. SAM, circularly polarized, makes it spin, while OAM, due to a helicoidal phase structure, makes it rotates around the propagation axis.

According to the definition of angular momentum, SAM and OAM can exist only if the light beam has azimuthal momentum in the transverse plane: $\mathbf{p}_\theta \neq 0$. Thus plane

waves, whose momentum is collinear with the direction of propagation due to the phase structure consisting of by infinite parallel planes, cannot carry any angular momentum. Yet, in practice plane waves do not exist: light beams are collimated in free space or confined as they propagate within the waveguide core. Furthermore, they are always being observed and measured with system of finite apertures. Therefore light beams can be manipulated in polarization for SAM or phase structure for OAM.

The previous condition on \mathbf{p}_θ implies also that \mathbf{E} and \mathbf{B} have a projection in the direction of propagation, $E_x \neq 0 \vee H_x \neq 0$, as a propagating e.m. field is formed by $(\mathbf{k}, \mathbf{E}, \mathbf{H})$ orthogonal each others. In the case of OAM, all the requirements on \mathbf{E} , \mathbf{B} and \mathbf{p}_θ are taken into account by the Poynting vector \mathbf{P} , which indicates the density flux of energy of the beam and is by definition parallel to the momentum: $\mathbf{P} = \mathbf{E} \times \mathbf{B}$. As fig. 3.2 on the right illustrates, in OAM beams the Poynting vector skews around the beam axis during propagation. At a given transverse plane, a circular flux of energy would be observed as a result of \mathbf{p}_θ . On the other hand, in the case of plane waves the Poynting vector is always parallel to the direction of propagation, so no OAM can be carried (fig. 3.2, left).

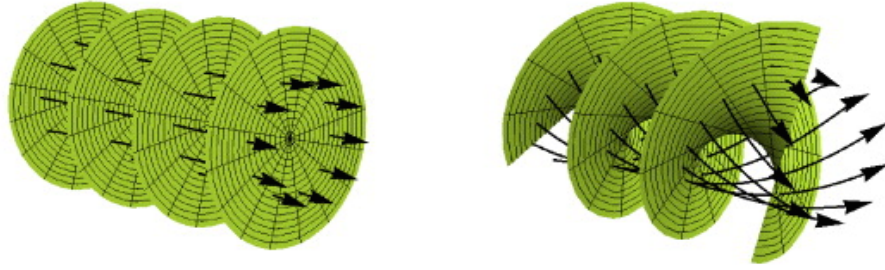


Figure 3.2: Comparison of wavefronts in the case of a plane wave beam (left) and a beam carrying OAM (right). The former one has constant phase surfaces, while the latter one posses a helicoidal phase structure, as highlighted by the skewing Poynting vector.

From this conclusion it is easy to understand the definition of angular momentum of light: $\mathbf{J} = \epsilon_0 \int \mathbf{r} \times (\mathbf{E} \times \mathbf{B}) d^3\mathbf{r}$. The same expression can also be derived from the Noether's theorem [7, 8], which returns an AM of light divided into two separate terms: $\mathbf{J} = \epsilon_0 \int (\mathbf{E} \times \mathbf{A}) d^3\mathbf{r} + \epsilon_0 \sum_{i=x,y,z} \int (E^i (\mathbf{r} \times \nabla) A^i) d^3\mathbf{r}$.

The first contribution refers to the possibility of a light beam to spin and carry spin angular momentum (SAM), while the second one to twist and carry orbital angular momentum (OAM).

3.2 Spin Angular Momentum

SAM is carried by circularly polarized (CP) light beams, in which the polarization vector rotates as the light propagates (fig. 3.1 (a)), as Poynting demonstrated at the beginning of 1900 [22]. Indeed, CP light beams with a radially decreasing intensity profile satisfies $\mathbf{L}_s = \mathbf{r} \times \mathbf{p} \neq 0$ [14] and a CP photon carries an unit of SAM: $L_s = \hbar$ [30]. The sign of L_s reflects the CP rotation verse, also known as handedness. From the point of view of the

detector, oriented towards the light source, right handed CP beams have $L_s = \hbar$, while left handed $L_s = -\hbar$.

A circular polarization state of the beam can be described as the superposition of two orthogonal linearly polarized states, delayed each other by a $\frac{\pi}{2}$ phase shift (fig. 3.1 (b)). Therefore CP beams can be obtained from orthogonal LP beams originating from the same source, as occurs in a quarter-wave plate (QW). A LP beam impinges on the QW at 45° with the optic axis, equally exciting two orthogonally polarized states. Due to birefringence, the orthogonal modes propagate through the QW with different effective refractive index and thus velocity, accumulating a phase delay. By properly choosing the QW plate length, their relative delay can be tuned exactly to $\frac{\pi}{2}$. As we will see in the next section, an analogous mechanism can be used to generate a light beam carrying an orbital angular momentum of first order.

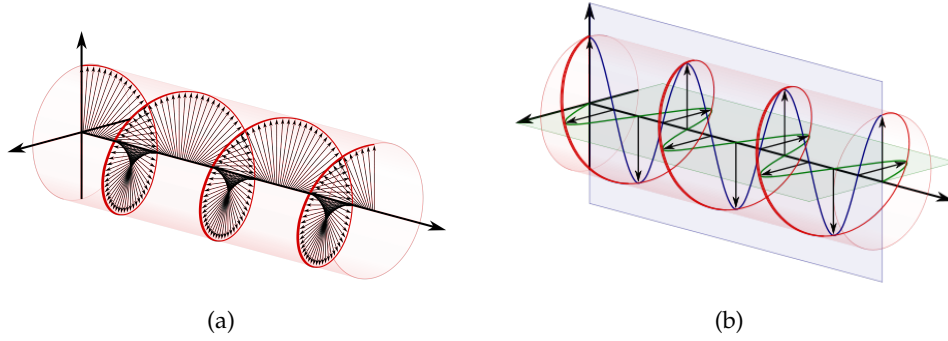


Figure 3.3: SAM light beam, also known as CP beam. As (a) shows, each polarization vector spins during propagation. (b) A CP beam can be decomposed into a TE and a TM beam, relatively delayed by a $\frac{\pi}{2}$ phase shift.

3.3 Orbital Angular Momentum

Orbital angular momentum (OAM) of light was proposed for the first time by Darwin in 1932 in order to explain quadrupole transitions in atoms [10]. In a quadrupole transition the absorption of one photon increases the atomic angular momentum by $2\hbar$, so it cannot be induced solely by a CP photon carrying SAM ($L_s = \hbar$). More generally, multipole transitions involving $\Delta L = \gamma\hbar$ can be explained only by supposing that photon has an OAM of $L_o = (\gamma - 1)\hbar$ in addition to SAM. However, the form of light beams carrying OAM was unknown until 1992, when Allen demonstrated that Laguerre-Gaussian (LG) modes carry a well-defined value of OAM [2]:

$$u(r, \phi, z) = \frac{C_{lp}^{LG}}{w(z)} \left(\frac{r\sqrt{2}}{w(z)} \right)^{|l|} \exp\left(-\frac{r^2}{w^2(z)}\right) L_p^{|l|} \left(\frac{2r^2}{w^2(z)} \right) \exp\left(-ik\frac{r^2}{2R(z)}\right) \exp(il\phi) \exp[i(2p + |l| + 1)\zeta(z)] \quad (3.1)$$

Such modes possess a helicoidal phase structure, expressed by the term $\exp(il\phi)$, where l is the azimuthal mode index. As the beam propagates, this helicoidal phase structure rotates so that each photon carries an OAM of $L_o = \pm l\hbar$, with l is the azimuthal index of the LG modes, also named orbital order.

Both OAM and SAM are quantized in unit of \hbar because in both cases the discretization of AM arises from the beam invariance to rotation around its axis. However, we underline that OAM has nothing to do with polarization and so with SAM. Rather, OAM arises from the spatial distribution of the beam and for such reason it is a new degree of freedom for light, in addition to polarization. On the contrary to SAM, which allows only the two orthogonal states right ($L_s = \hbar$) and left handed CP ($L_s = -\hbar$), OAM has a set of infinite set of eigenstates $L = \pm l\hbar$ and thus a single OAM photon can transmit a much richer information.

Fig. 3.2 compares the helicoidal spatial distributions of a LG beam, associated to an OAM of $L_o = \hbar$, with the one of a traditional beam, given by parallel planes.

The helicoidal phase structures explains the reason for the discretization of OAM in unit of \hbar . Since either \mathbf{E} or \mathbf{H} exist out of plane, \mathbf{p} has an azimuthal component $\mathbf{p}_\phi = \hbar k_0 \cos(\theta) = \hbar k_0 \frac{l\lambda}{2\pi r}$, where θ is the inclination of the phase front, and thus Poynting vector, with respect to the beam axis.

The effect of this skewing energy flux is straightforward: if an OAM were shone on you, it would exert a torque, while a common light beam would just push you away.

If we record the propagating phase structure at a fixed transverse plane, we would obtain a helicoidal phase profile. As fig. 3.4 shows, the phase changes only azimuthally by $2l\pi$, where l is the LG azimuthal index that defines the number of helices per wavelength and thus the order of carried OAM. As l increases, the phase structure evolves from parallel planes ($l = 0$), to a helicoidal surface ($l = \pm 1$) and two intertwined helicoidal surfaces ($l = \pm 2$).

A direct consequence of the helicoidal phase profile is a donut shaped intensity profile. Indeed, at the beam axis the phase has a singularity [40, 29] and thus it cannot be defined, as for the time zone at the centre of the North Pole [41]. As result, the intensity is zero at the center of the beam, where there is a dark vortex called optical vortex. The optical vortex is defined according to its topological charge l , equal to the OAM order, and does not carry any energy and thus OAM. If we consider the whole phase structure of the beam, the phase singularity coincides with the line of the beam propagation axis. Therefore, the beam energy and thus momentum (both linear and orbital) is not carried at the beam axis, where there is no light. We can see in fig. 3.4, on the right, that the intensity increases radially from the beam center, with a polynomial growth as predicted by eq. 3.1.

3.3.1 HG to LG transformation

There are several ways to generate an OAM beam of light. The most common are based on spiral phase plates [6, 38, 25, 35], forked diffractive gratings and computer generated holograms [5, 15, 4, 34] and q-plates [24, 17]. However, these methods cannot be implemented in integrated optics, given the limitation imposed by growth, patterning and etching fabrication steps. For such purpose there is only one suitable method,

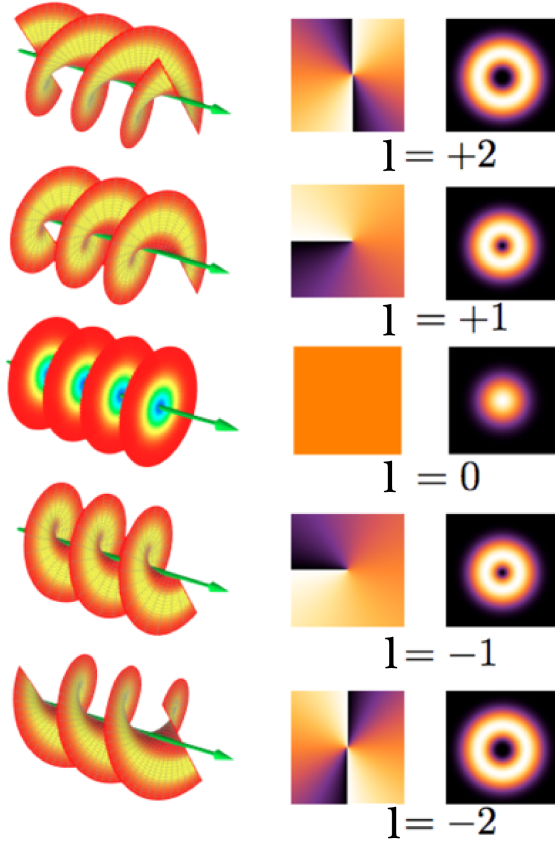


Figure 3.4: Phase structure, phase profile and intensity of the first two orders OAM light: $l \in [2, -2]$. In $l = 0$ case, the phase structure is made by disconnected surfaces (e.g. parallel plane in plane waves) and no OAM is carried. If $l = \pm 1$, the phase structure is a single helical surface, whose step length is given by the wavelength λ . For higher order modes $l > 1$, the wavefront is composed by l intertwined helices, whose step length is $\frac{\lambda}{l}$. The helical phase structure rotation verse reflects the sign of l , as can be observed for $l > 0$ and $l < 0$.

named cylindrical mode conversion of Hermite-Gaussian (HG) to Laguerre-Gaussian (LG) beams. Incidentally, this method was also the first one proposed by Allen in 1992 [2].

An OAM beam can be decomposed in a specific number of HG beams, described by eq. 3.2, each one with a properly phase delay.

$$u_n(x, z) = \left(\frac{2}{\pi}\right)^{1/4} \left(\frac{1}{2^n n! w_0}\right)^{1/2} \left(\frac{q_0}{q(z)}\right)^{1/2} \left[\frac{q_0 q^*(z)}{q_0^* q(z)}\right]^{n/2} H_n\left(\frac{\sqrt{2}x}{w(z)}\right) \exp\left[-i\frac{kx^2}{2q(z)}\right] \quad (3.2)$$

The previous transformation is possible because both HG and LG form a complete set of solutions for the Helmholtz equation, in cartesian and cylindrical coordinates respectively. In particular, Hermite polynomials are related to Laguerre polynomials [1] by eq. 3.3:

$$\sum_k^{m+n} = (2i)^k P_k^{(n-k, m-k)}(0) H_{(n+m-k, 0)} H_{(0, k)} = 2^{(n+m)} (-1)^n (x - iy)^{(m-n)} L_n^{(m-n)}(x^2 + y^2) \quad (3.3)$$

Since we are interested in generating an OAM of first order, we consider the case of first order Hermit polynomials, for which $m = 1$ and $n = 0$. The previous relation reduces to:

$$H_{1,0}(x) - iH_{0,1}(y) = 2(x - iy)L_0^1(x^2 + y^2) \quad (3.4)$$

Given the definition of LG (eq. 3.1) and HG modes (eq. 3.2), we can rewrite eq. 3.4 in terms of corresponding modes. The resulting HG into LG conversion for first order OAM is summarized by: eq. 3.5.

$$LG_{(0,1)} = HG_{1,0} + iHG_{0,1} = HG_{1,0} + e^{i\frac{\pi}{2}} HG_{0,1} \quad (3.5)$$

According to the derived conversion, illustrated in fig. 3.5, a LG mode carrying an OAM of the first order ($l = 1$) can be obtained by superposing one $HG_{(1,0)}$ mode, first order along the horizontal direction, and one $HG_{(0,1)}$ mode, first order along the vertical direction, with the latter one delayed by a $\frac{\pi}{2}$ phase shift. If the relative phase delay is $-\frac{\pi}{2}$, the resulting LG beam would carry an OAM of $l = -1$ instead of $l = 1$.

3.3.2 Generation of an OAM light beam in a waveguide

The HG to LG conversion, also known as $\frac{\pi}{2}$ -converter after the required phase delay, can be implemented in free space by a pair of cylindrical lenses [2]. Still, this kind of conversion is not commonly used to generate OAM light beams as first order HG modes cannot be easily emitted by laser sources. On the other hand, in a waveguide the HG to LG conversion can be implemented, as Liang has recently demonstrated for a hybrid SOI/plasmonic waveguide [21]. If the core of the waveguide is chosen small enough, the two fundamental quasi-TE and quasi-TM modes present a not negligible electric field along the direction of propagation. The two E_x components are orthogonal HG first order modes, according to eq. 3.6.

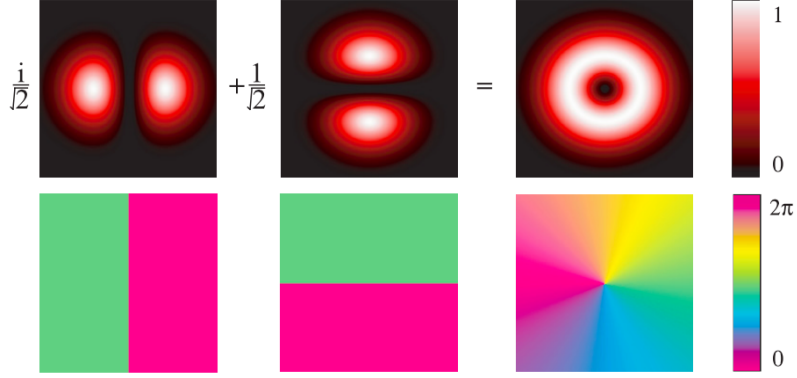


Figure 3.5: HG first order modes $HG_{(1,0)}$ and $HG_{(0,1)}$, delayed each other by a $\frac{\pi}{2}$ phase shift, superpose to give a LG light beam that carries OAM $l = 1$.

$$E_x = \frac{1}{i\beta} \nabla_T E_T$$

which for quasi-TE and quasi-TM can be rewritten as:

$$E_{x,TE} \approx i \frac{dE_y^{TE}}{dy}$$

$$E_{x,TM} \approx i \frac{dE_z^{TM}}{dz}$$

(3.6)

These two modes are equally excited by an input beam linearly polarized (LP) at 45° and $\frac{\pi}{2}$ phase shifted by a plasmonic layer of Cu. In this way a light beam carrying $OAM_{l=1}$ can be generated.

However, despite the brilliant idea to generate OAM through the E_x component of the modes, Liang's SOI/hybrid waveguide has not been fabricated. The main reason is probably related to the complexity of the waveguide structure. In addition to the usual fabrication steps, SiO_2 thermal oxidation and Cu deposition are required, preceded by the corresponding alignment steps. Besides, as the generated OAM depends strongly on the birefringence of the hybrid SOI/delay section, there are some demanding tolerances in the waveguide geometry. As a result, only a phase shift of $\frac{\pi}{2} \pm \frac{\pi}{8}$ is achievable, while an exact phase shift of $\frac{\pi}{2}$ is mandatory to generate a well-defined OAM light beam.

4 OAM/SAM light beam generated by a AlGaAs on-chip mode converter

4.1 AlGaAs based device

Inspired by Liang's idea [21], we aim to design a device that converts a 45° LP beam into a beam carrying opposite OAM and SAM. Instead of SOI, we choose to conceive a device based on AlGaAs, taking advantage of the DON team expertise in the fabrication of AlGaAs waveguides. Besides, an AlGaAs device can eventually achieve laser emission, thanks to the direct band gap, or χ^2 non linear photon pair sources, given the symmetric crystal lattice. Regarding the conception of the device, the choice of AlGaAs imposes more restrictions to the design than SOI. The reason is that a high index contrast helps the confinement of light in a waveguide. At the telecom wavelength SOI offers $\Delta n_{SOI} = n_{SI} - n_{SiO_2} = 3.478 - 1.444 = 2.034$, while AlGaAs only $\Delta n_{AlGaAs} = n_{GaAs} - n_{AlGaAs_{min}} = 3.37 - 2.98 = 0.39$. But, on the other hand, AlGaAs is more versatile, as the percentage of Al atoms (x) in comparison to Ga ($1 - x$) can be tuned during the growth process of an $Al_xGa_{1-x}As$ layer.

As fig. 4.1 illustrates, at the telecom wavelength, the available refractive index range is $[2.98, 3.37]$ and n_{AlGaAs} decreases with the percentage of Al x . The minimum value $n_{AlGaAs_{min}} = 2.98$ corresponds to an Al percentage of 80%. $Al_xGa_{1-x}As$ layers with $x > 0.8$ cannot be fabricated because afterwards oxidation would occur and the waveguide structure and surfaces would be damaged.

Pure GaAs ($x = 0$) presents the highest refractive index ($n_{GaAs} = 3.37$), which usually determines the core of the waveguide where the light, confined, propagates.

Since GaAs is the substrate on which the growth occurs, one or more layers of $Al_xGa_{1-x}As$ need to be placed between the core guiding region and the substrate to avoid leaking and consequent propagation losses.

4.2 Design guidelines

The AlGaAs device must be designed to fulfil several requirements. Firstly, the physical conditions necessary for the generation of an OAM light beam need to be satisfied. Secondly, in view of the future characterization of the device, the emitted OAM must be sufficiently powerful, with no other signals superposed to it. Therefore we need to optimize the device conversion efficiency. Lastly, there are some technical and fabrication related tolerances to be respected. In this section we present in details all these three kind of requirements, necessary to understand the proposed device structure (sect. 4.3) and the performed optimization (ch. 5).

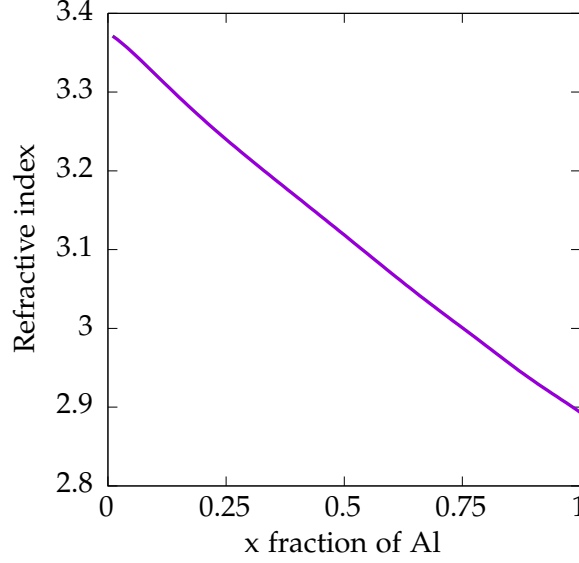


Figure 4.1: The refractive index of $Al_xGa_{1-x}As$ decreases with the percentage of Al, within the range $[2.98, 3.37]$.

4.2.1 OAM generation

Firstly, an OAM light beam is rotational invariant and so requires a symmetric waveguide. Since in the waveguide the OAM is generated on the E_x component of modes, we ask that $E_x^{quasi-TE}(y, z)$ has the same spatial distribution and amplitude of $E_x^{quasi-TM}(y, z)$ rotated by 90° . Also, a light beam of $OAM_{l=1}$ is well defined only if the $HG_{(1,0)}$ and $HG_{(0,1)}$ are phase shifted exactly by $\frac{\pi}{2}$. On the contrary, the light beam would decompose in the two separate modes $HG_{(1,0)}$ and $HG_{(0,1)}$ during its propagation. For this reason we need to take care that the device delay section L_{delay} , responsible for the $\frac{\pi}{2}$ phase shift, is achieved with as much accuracy as possible.

4.2.2 Conversion efficiency

Once the conditions for the generation of OAM are satisfied, we consider the conversion efficiency. The conversion efficiency is the portion of energy at the input of the device that is converted into the OAM light beam. The device has high efficiency if works in monomode condition, with high coupling at the input and a sufficiently small diffraction angle at the output. Such features will allow, given an incoming gaussian beam LP at 45° , an easy collection and detection of the emitted OAM beam. Besides, since OAM is carried by the longitudinal component of the electric field, in the generated beam the ratio between E_x and the transverse mode component E_t should be as high as possible. This will permit to detect the OAM beam with sufficient visibility.

4.2.3 Fabrication tolerances

At last, in order to have a high yield in the fabrication process, we have studied the tolerances on the structure and geometry of the waveguide. The growth of the wafer,

obtained by molecular beam epitaxy (MBE), presents an uncertainty of $\Delta x = 5\%$ in the percentage of Al for every grown $Al_xGa_{1-x}As$ layer. The tolerance in the composition of $Al_xGa_{1-x}As$ implies a tolerance on its effective index $\Delta n = \pm 0.03$. Therefore we need to take care that the monomode condition and the induced phase delay are not affected by this uncertainty on the composition of $Al_xGa_{1-x}As$. The lithography can be performed by either photolithography (PL) or electron beam lithography (EBL). The choice of one of the other relies mostly on the size and accuracy of the features to fabricate. PL is very fast but can only pattern waveguide larger than $3\mu m$ with an uncertainty of $\Delta w = \pm 300nm$ on their width. On the contrary, EBL can pattern even very small features with a width tolerance of $\Delta w = \pm 10nm$, at the price of a very slow speed. However, for large and long straight waveguide, EBL Fixed Beam Moving Stage mode can be activated and the fabrication speed is no longer an issue. The patterning is followed by Inductively Coupled Plasma (ICP) physical etching, which gives an error of about $\pm 50nm$ in the etched height. This error should not invalidate the OAM requirements or worsen the conversion efficiency, as the waveguide core dimensions largely exceeds $50nm$. The last operation is the mechanical cleaving, which defines the device length along the direction of propagation of light. Manual cleaving assures at maximum a $100\mu m$ accuracy on the device length. As we will see, this uncertainty is unbearable for the length of the $\Delta = \frac{\pi}{2}$ delay section, which therefore cannot be placed at the device input or output.

All the discussed requirements are summarized in the following tables:

OAM generation	Conversion efficiency
symmetric waveguide	monomode
L_{delay} to give $\pi/2$ delay	low propagation losses
$E_x^{TE}(y, z) = E_x^{TM}(y, z)$ rotated by 90°	high and easy input coupling
	low diffraction output
	high E_x/E_t

Table 4.1: OAM and conversion efficiency requirements.

Fabrication tolerances	Step
composition: $\Delta x = 5\%$ in $Al_xGa_{1-x}As$	<i>Growth</i>
width: $\pm 300nm$ in PL, $\pm 100nm$ in ECP, $\pm 10nm$ in EBL	<i>Patterning</i>
height: $\pm 50nm$ in ICP dry etching	<i>Etching</i>
length: at least $\pm 100\mu m$ for manual mechanical cleaving	<i>Cleaving</i>

Table 4.2: Fabrication feasibility and corresponding fabrication step.

4.3 Device structure

To satisfy all the given requirements, we have investigated several waveguides designs. We started from waveguide structures which could be fabricated by PL. Since standard PL cannot be used to fabricate small features, we limited our study to waveguides with

large core widths ($w > 3\mu\text{m}$). However, as the number of guided modes increases with the size of the core, the monomode condition is hard to satisfy. An exception to this common rule is given by rib waveguides, which allow monomode condition even for $L > 3\mu\text{m}$ [33]. Unfortunately, we observed that large core widths do not permit to satisfy the conversion requirement of high $\frac{E_x}{E_t}$. Furthermore, the mode presents an elliptical shape, so also the OAM condition of rotational invariance is not verified by rib waveguides.

Among the investigated waveguide structures, a wire waveguide appears to be the best one, as it fulfils all the indicated requirements.

In the wire waveguide, illustrated in fig. 4.2, the light propagates within the core (GaAs), a region located on the top and with the highest refractive index. The core is separated from the underlying substrate (GaAs) by a cladding layer ($\text{Al}_{0.8}\text{Ga}_{0.2}\text{As}$), while is surrounded by air ($n = 1$) in the other directions.

The square shape of the core region satisfies the OAM rotational symmetry, as $E_x^{TE}(y, z) = E_x^{TM}(y, z)$ rotated by 90° . Furthermore, the difference in refractive index between the core ($n = 3.37$ for GaAs) and the surrounding layers ($n = 1$ and $n_{clad} = 2.98$), for sufficiently small core dimension, leads to an acceptable $\frac{E_x}{E_t}$ ratio.

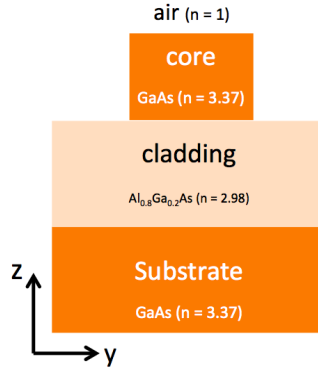


Figure 4.2: Wire AlGaAs waveguide structure and composition

4.3.1 Layers composition

To avoid the leakage of the guided modes into the substrate of GaAs ($n = 3.37$), the refractive index of the cladding layer is chosen as low as possible: $n_{clad} = n_{\text{Al}_{0.8}\text{Ga}_{0.2}\text{As}} = 2.98$.

The waveguide layers composition, with the corresponding Al percentage and refractive index, is indicated in fig. 4.2.

4.3.2 Geometry

Once the waveguide layers and materials are defined, we proceed to the optimization of the geometrical parameters. We need to set the cladding thickness, core width and etched height of the wire waveguide. Since the device has many constraints to satisfy,

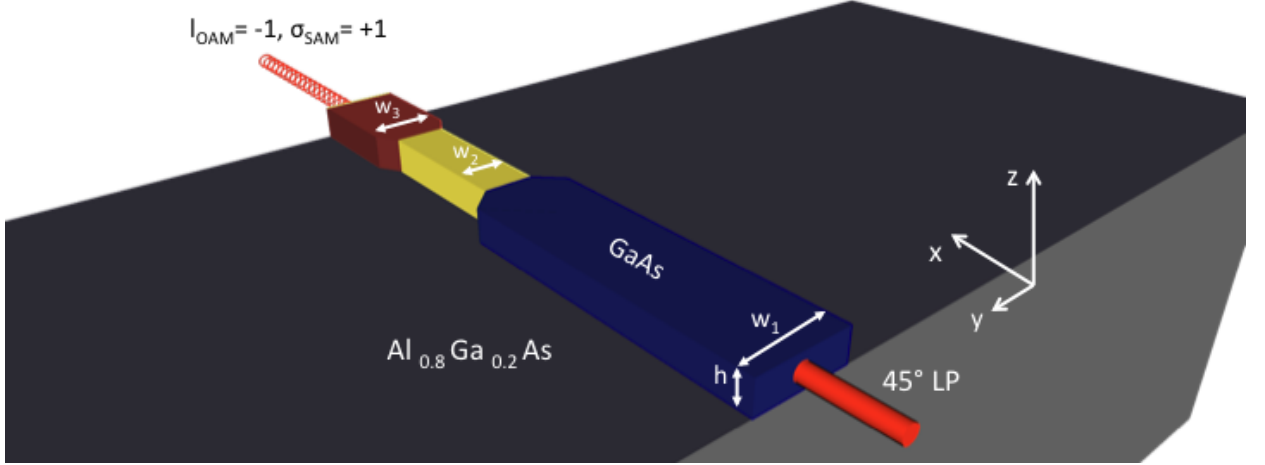


Figure 4.3: *AlGaAs* LP to SAM/OAM device structure. The thickness of the core is $h = 1.08\mu\text{m}$, while its width changes in the three sections: $w_1 = 3\mu\text{m}$, $w_2 = 0.55\mu\text{m}$ and $w_3 = 1.08\mu\text{m}$. The first section maximises the input coupling, the second one generates the OAM/SAM and the last one improves the rotational symmetry of the beam and assures a small diffraction angle.

we divide the waveguide into three different sections, each one with a specific goal, as illustrated in fig. 4.3.

The input section (blue in the figure) allows a high input coupling efficiency, the middle one (yellow) generates the OAM/SAM beam and the output part (red) assures rotational symmetry and a small diffraction angle. The resulting OAM in the output section, calculated from eigenmode simulations, is shown in fig. 4.4. As we can see, the fundamental modes are two orthogonal first order HG modes along the longitudinal component of the electric field (4.4 a,b). As predicated by the HG to LG conversion, when these two modes superpose each other with a relative phase delay of $\frac{\pi}{2}$, an OAM light beam with its unique donut shape is achieved (4.4 c).

Each section performs an unique task because of a different core width. The input section (blue in fig. 4.3, (a) in fig. 4.5) has a large core width of $w = 3\mu\text{m}$. Therefore an incoming beam, linearly polarised (LP) at 45° and with a beam waist of $\approx 3\mu\text{m}$, couples with the waveguide fundamental modes with high efficiency.

4.4 $\frac{\pi}{2}$ phase-shift by use of an asymmetric waveguide

Regarding the delay section (yellow part in fig. 4.3, (b) in fig. 4.5), to further reduce the device losses and simplify the fabrication process, instead of a plasmonic layer, we propose a new way to obtain the desired $\frac{\pi}{2}$ phase shift between the quasi-TE and quasi-TM modes. By definition, the quasi-TE highest electric field component, E_y , is perpendicular to the quasi-TM highest field component, E_z . Therefore an asymmetric wire waveguide core makes the two modes propagate with different effective index n_{eff} , and thus phase velocity, according to $v_{phase} = \frac{c}{n_{eff}}$.

In particular, the core width $w_{delay} = 0.55\mu\text{m}$ is chosen to be approximately half

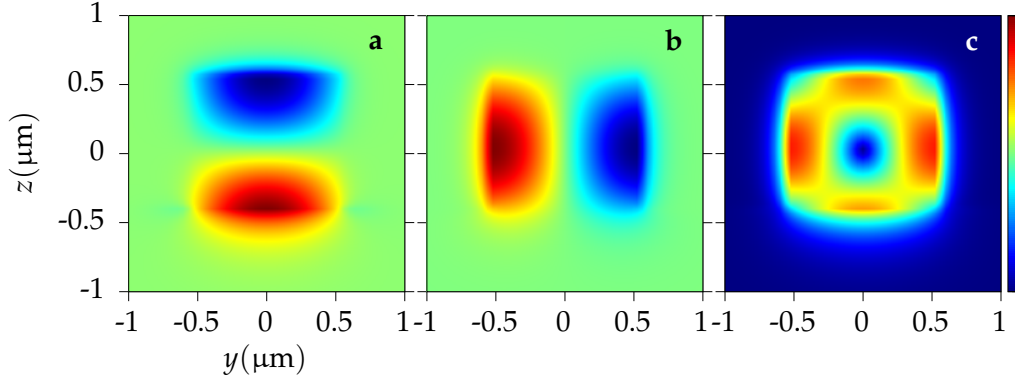


Figure 4.4: $E_x(y, z)$ (real part) for the two fundamental modes and their superposition in the device output section. The quasi-TE (a) and quasi-TM (b) modes superpose with a relative delay of $\frac{\pi}{2}$, matured in the delay section. As result an OAM light beam (c) is generated.

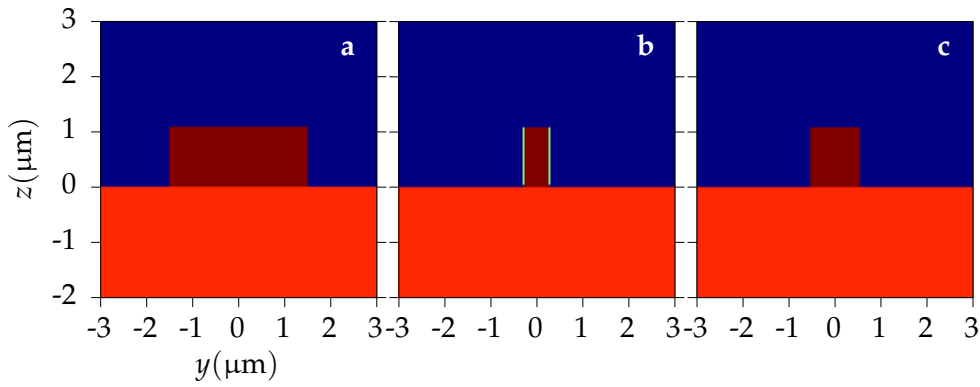


Figure 4.5: AlGaAs device geometry and refractive index profile of input (a), delay (b) and output section (c).

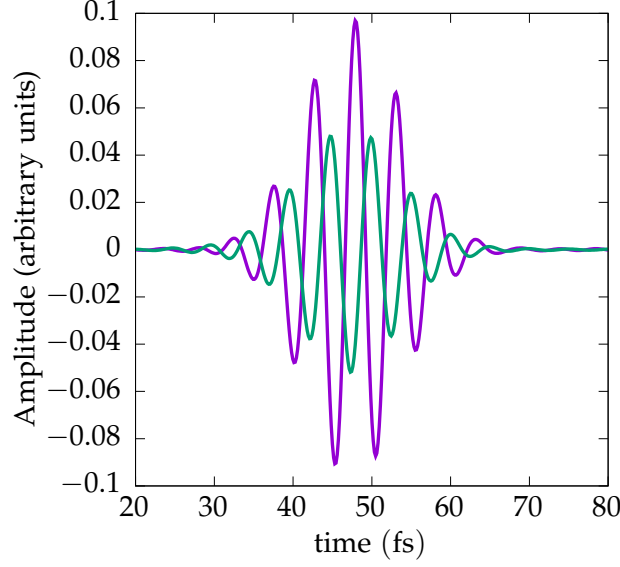


Figure 4.6: TE (in violet) and TM (in green) components of the generated OAM beam, in function of time. Since TE precedes TM by a $\pi/2$ phase shift, the generated beam carries a SAM of $L_{SAM} = -\hbar$.

of the core height $h = 1.08\mu\text{m}$ (fig. 4.5 (b)). As a consequence, the quasi-TM mode ($n_{TM} = 3.121$) travels slower than the quasi-TE mode ($n_{TE} = 3.020$). After a propagation length L_{delay} , the quasi-TM mode accumulates a phase delay of: $\Delta = \frac{2\pi}{\lambda} \Delta n_{eff} L_{delay}$. Given $\Delta n_{eff} = n_{TE} - n_{TM} = 0.101$, a length section long $L_{delay} = 38.366\mu\text{m}$ induces the $\frac{\pi}{2}$ phase shift and a beam carrying OAM is generated. Since the fundamental modes are orthogonally polarised, we expect the delay section to act as a quarter-wave plate as well. Fig. 4.6 presents the transverse component of the total field at the end of the delay section, calculated via a FDTD simulation. We can clearly see that the y component of the field, given by the quasi-TE mode, is $\frac{\pi}{2}$ delayed from the z component, given by the quasi-TM mode. Therefore the field is circularly polarized and carries SAM equal to $L_{SAM} = -\hbar$.

confirms that the generated beam is circularly also polarized and carries a SAM opposite to OAM. The total momentum of zero is thus conserved and no torque is exerted by the waveguide on the propagating beam.

The last section, named output section (red part in fig. 4.3, (c) in fig. 4.5)), is optimised to improve the rotational symmetry of the OAM mode and make it diffract at an acceptable diffraction angle. For this purpose a square core is used (circular waveguides are not feasible with the conventional patterning techniques). The reason is that $w_3 = h$ assures also that the two HG modes do not accumulate any other phase shift in addition to the $\frac{\pi}{2}$ previously matured. Their amplitude are almost the same, but not exactly because the core boundaries are not symmetric: along the horizontal direction the core is surrounded by air ($n = 1$) on both sides, but in the vertical direction air is only above, as below there is a cladding of $n_{clad} = 2.98$. As $\Delta n_{core-air}$ is bigger than $\Delta n_{core-cladding}$, the mode is more confined in the horizontal direction (quasi-TE) than in the vertical one (quasi-TM). So the amplitude of $E_x^{quasi-TE}(y, z)$ is bigger than $E_x^{quasi-TM}(y, z)$ by a factor

of ≈ 1.17 .

At last, the three sections are coupled without losses thanks to two adiabatic tapers. As fig. 4.3 shows, the first one is a bottleneck, which slowly narrows from 3 to $0.55\mu\text{m}$, while the second one is a gradual aperture from $0.55\mu\text{m}$ to $1.08\mu\text{m}$. As long as the later dimension of the tapers changes adiabatically, the light travels through them without being back-reflected or scattered.

4.5 OAM/SAM beam at the output of the device

As discussed in the introduction about OAM (section 3.3), a beam of light carries OAM if it has a helicoidal phase structure. Thus on a transverse plane, the OAM beam presents a helicoidal phase profile and a donut spatial distribution of the intensity.

In our AlGaAs device OAM is generated through the E_x component of the field, so we study the $E_x(y, z)$ phase profile and spatial distribution in the near field ($d \approx \frac{\lambda}{3}$ from the waveguide output facet), presented in fig. 4.7.

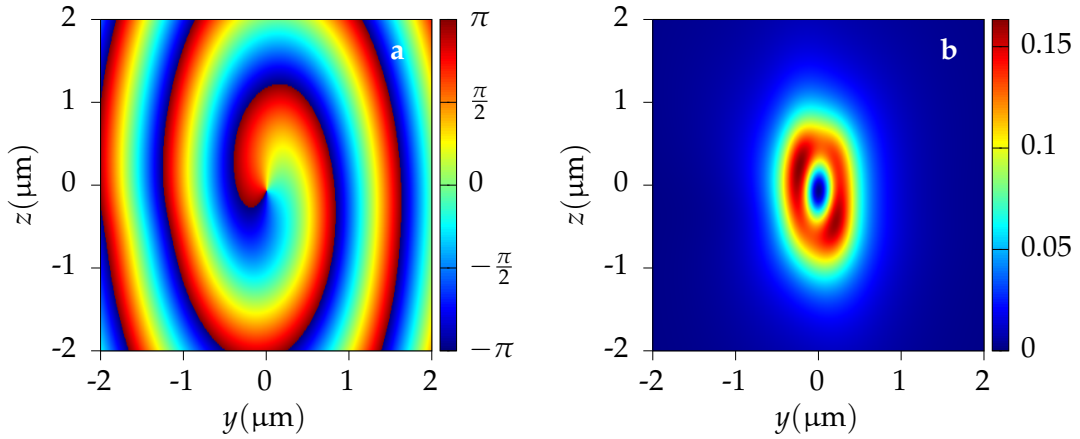


Figure 4.7: Study of $E_x(y, z)$ of the emitted beam proves that it carries OAM, as evinced by the helicoidal phase profile (a) and intensity distribution (b).

As we can see from the helicoidal phase profile, whose azimuthal periodicity is $p = 2\pi l = 2\pi$, and the donut intensity distribution of the field, given by the optical vortex, the beam is Laguerre-Gaussian $LG_{(0,1)}$ carrying OAM $l = 1$.

An additional indication that the beam carries OAM is given by its Poynting vector $\mathbf{P}(\mathbf{x}, \mathbf{y}, \mathbf{z})$, which skews around the beam axis (fig. 3.2) as the light beam propagates. For this reason OAM beams are also called "twisted" beams. Thus if we look at the transverse component of the Poynting vector at a given transverse plane, $\mathbf{P}_t(\mathbf{y}, \mathbf{z})$, we should observe that it rotates along the azimuthal direction. However, at the device output the light beam is also diffracting, so $\mathbf{P}_t(\mathbf{y}, \mathbf{z})$ has a radial component as well. To highlight the rotation of the beam, we filter this background noise due to diffraction. The resulting $\mathbf{P}_t(\mathbf{y}, \mathbf{z})$ is shown in fig. 4.8. As expected $\mathbf{P}_t(\mathbf{y}, \mathbf{z})$ rotates along the azimuthal direction. Besides, the intensity profile shows that no energy is carried by $\mathbf{P}_t(\mathbf{y}, \mathbf{z})$ along the beam axis, a further confirmation of the presence of the OAM optical vortex.

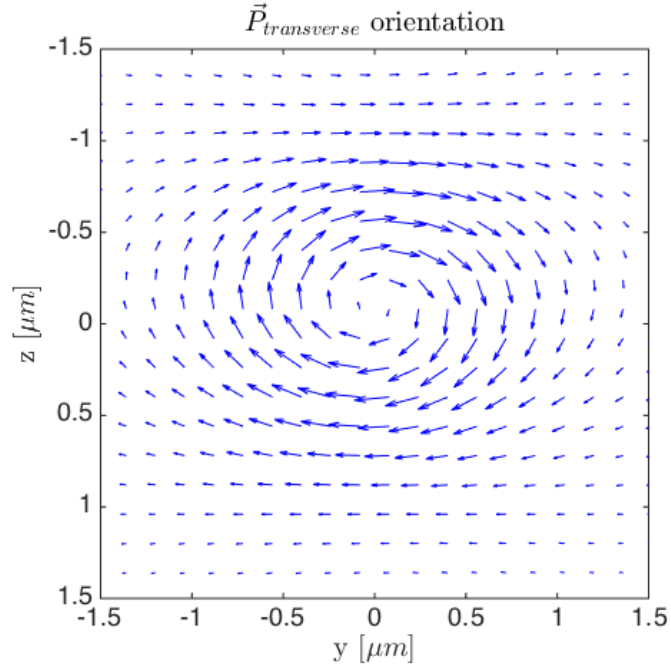
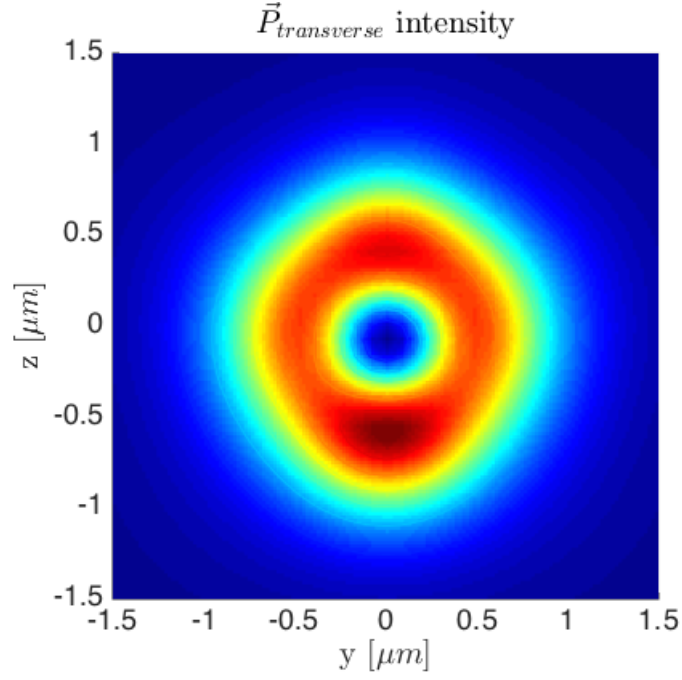


Figure 4.8: Study of the Poynting vector of the emitted beam shows that it is rotating around the propagation axis. This can be understood from its intensity profile (a) and orientation (b) of its transverse component $\mathbf{P}_t(y, z)$.

5 Device optimization and tolerances study

5.1 Input Coupling

As in electronics, where a portion of the signal power can be reflected at an interface between two components with different impedances, in optics a light beam can be partially reflected as it encounters a change in refractive index. This occurs at the wafered input facet, where the beam propagates from air to AlGaAs, experiencing a refractive index contrast of $\Delta n \approx 2$. The fraction of light power that is not reflected couples into the waveguide, where it distributes among the eigenmodes according to the mode coupling theory. The overlaps (eq. 5.1) between the incoming beam $(\mathbf{E}_1, \mathbf{H}_1)$ and each eigenmode $(\mathbf{E}_2, \mathbf{H}_2)$ determine which modes are excited in the waveguide.

$$\eta = \text{Re} \left\{ \frac{\int \mathbf{E}_1 \times \mathbf{H}_2^* \cdot d\mathbf{S} \int \mathbf{E}_2 \times \mathbf{H}_1^* \cdot d\mathbf{S}}{\int \mathbf{E}_1 \times \mathbf{H}_1^* \cdot d\mathbf{S}} \frac{1}{\text{Re} \left\{ \int \mathbf{E}_2 \times \mathbf{H}_2^* \cdot d\mathbf{S} \right\}} \right\} \quad (5.1)$$

Since in our device the OAM is carried by E_x , we require $E_x^{\text{quasi-TE}}(y, z) = E_x^{\text{quasi-TM}}(y, z)$ to generate a well-defined OAM beam. For such purpose, the incoming gaussian beam, generated by a laser source at $\lambda = 1.55\mu\text{m}$, is linearly polarized at an angle α with the optic axis, so that $\frac{E_x^{\text{quasi-TE}}(y, z)}{E_x^{\text{quasi-TM}}(y, z)} = \tan(\alpha) = 1$.

To ease the coupling, the core width ($w_1 = 3\mu\text{m}$) is chosen large enough in comparison with the beam waist of the incoming beam ($w_{\text{waist}} = 1.5\mu\text{m}$), as fig. 4.3 shows. The width w_1 can also bear the a tolerance of $\Delta w_1 \approx 100\text{nm}$, so FBMS EBL can be used instead of the slower EBL.

On the other hand, the core is large enough to support, in addition to the two fundamental ones (fig. 5.1 (b,c)), 15 higher order modes. The first three ones are represented in fig. 5.1 (d,e,f). As these higher order modes do not contribute to the generation of light OAM, they must not be excited. The power of the incoming beam that couples into them not only is lost, but it superposes to the generated SAM/OAM signal at the device output, like a noise.

If the incoming beam is perfectly aligned with the waveguide input facet this problem is avoided. Indeed, higher order modes $H_{(n,m)}$ present an electric field with a symmetric or antisymmetric spatial distribution, for n and m odd or even respectively. As they couple with an aligned incoming gaussian beam, whose beam spot covers the entire core facet ($w_d > w_1 = 3\mu\text{m}$), their lobes give opposite contributes in the calculation of the overlap integral (eq. 5.1).

At zero offset, the coupling is either zero for higher order odd modes or almost negligible for higher order even modes. Thus only the fundamental quasi-TE and quasi-TM modes are excited.

On the other hand, if the incoming beam is not perfectly centered with the input core

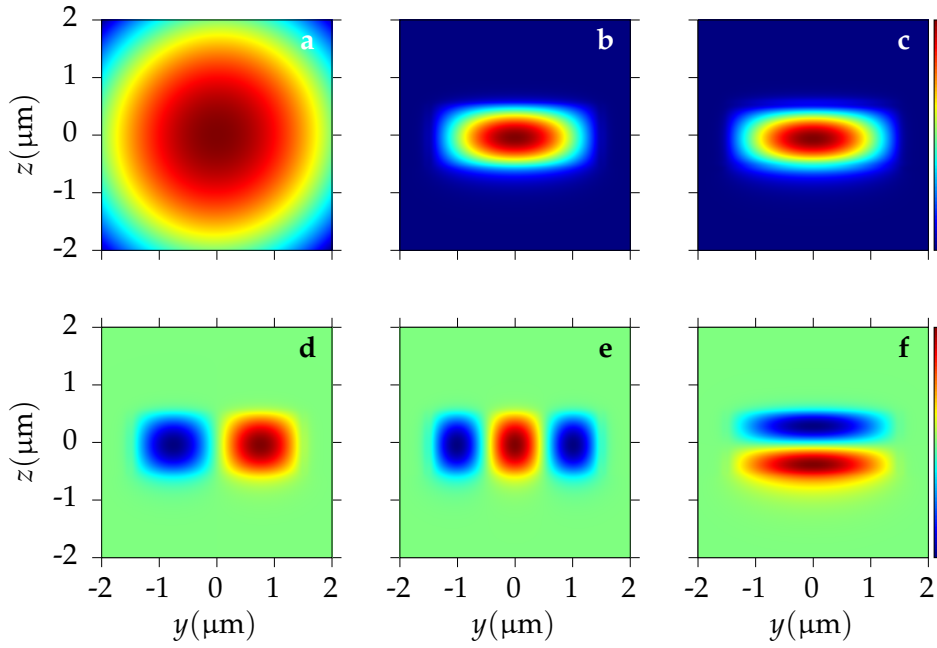


Figure 5.1: $E(y, z)$ (real part) of incoming gaussian mode of beam waist $w_r = 1.5\mu\text{m}$ (a) is compared with the two waveguide fundamental modes, orthogonally polarized, $H_{(0,0)}$ (b,c) and the first three higher order modes (d,e,f). At zero offset, the between the gaussian beam has a high overlap with the fundamental modes and a low overlap with the higher order modes, due to the symmetry of their spatial distribution.

facet, it may overlap more with the higher order modes than with the fundamental ones. This might be critical in practical measurements, as the piezo used for alignment has an offset tolerance of $\Delta x = \Delta y = \Delta z = 0.5\mu\text{m}$.

In addition to the offset, the input coupling depends on the beam numerical aperture NA . According to $NA = \text{atan}\frac{w(z)}{z}$, NA describes how much the beam spot $w(z)$ widens after it reaches its smallest value, named beam waist, at the focal plane (fig. 5.2)

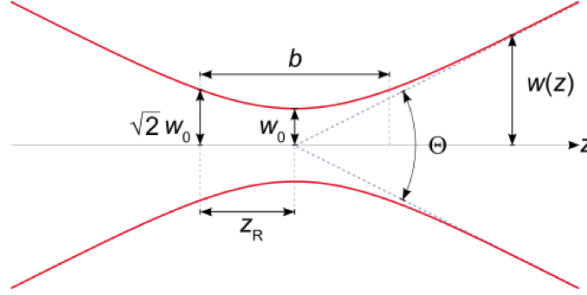


Figure 5.2: Focusing of a gaussian beam. $w(z)$ is beam spot size in function of its propagation position z . w_0 is the beam waist, the smallest spot size of the beam which occurs at the focal point.

Since we can use either a lens ($NA = 0.5$) or a microlens fiber ($NA = 0.123$) to collimate the laser spot on the waveguide facet, we compare the coupling performances and alignment tolerances in both cases via eigenmode simulations. In fig. 5.3 we compare the input power coupling in function of the offset for the lens and optical fiber.

As expected, the power coupling into the fundamental modes is maximised if the incoming gaussian beam is perfectly centred with the core facet. As the offset increases along y (or z), higher order modes $H_{(n,0)}$ (or $H_{(0,n)}$) are progressively more excited.

We also observe that the coupling efficiency increases with NA , while the tolerance in the coupling alignment decreases. As fig. 5.3 illustrates and table 5.1 summarizes, the lens provides a better power coupling efficiency ($\approx 0.45\%$ for $NA = 0.5$) than the optical fiber ($\approx 0.23\%$ for $NA = 0.123$), at the price of a smaller window for alignment ($0.5 \times 0.5\mu\text{m}^2$ VS $1 \times 1\mu\text{m}^2$).

Table 5.1: Comparison between lens and microlens fiber input coupling tolerances and performances.

	Alignement window [μm^2]	Power coupling $\frac{P_{\text{coupled}}}{P_{\text{incoming}}}$
Lens ($NA = 0.5$)	0.5×0.5	0.45
Microlens fiber ($NA=0.123$)	1×1	0.23

Since the 0.5×0.5 alignment window is feasible with the piezo, the lens will be employed to collimate the incoming beam on the waveguide input facet.

The same detailed study of alignment tolerances is not necessary along the direction of propagation x . In the lenses case, $Z_r = 4.5\mu\text{m}$, $w_r = 1.5\mu\text{m}$ and $\lambda = 1.55\mu\text{m}$, so according to $w(z)^2 = w_0^2 \left[1 + \left(\frac{\lambda z}{\pi w_0^2} \right)^2 \right]$ a significant widening of the beam spot size is not expected. A single simulation confirms that, in the lens case, a gaussian beam focused

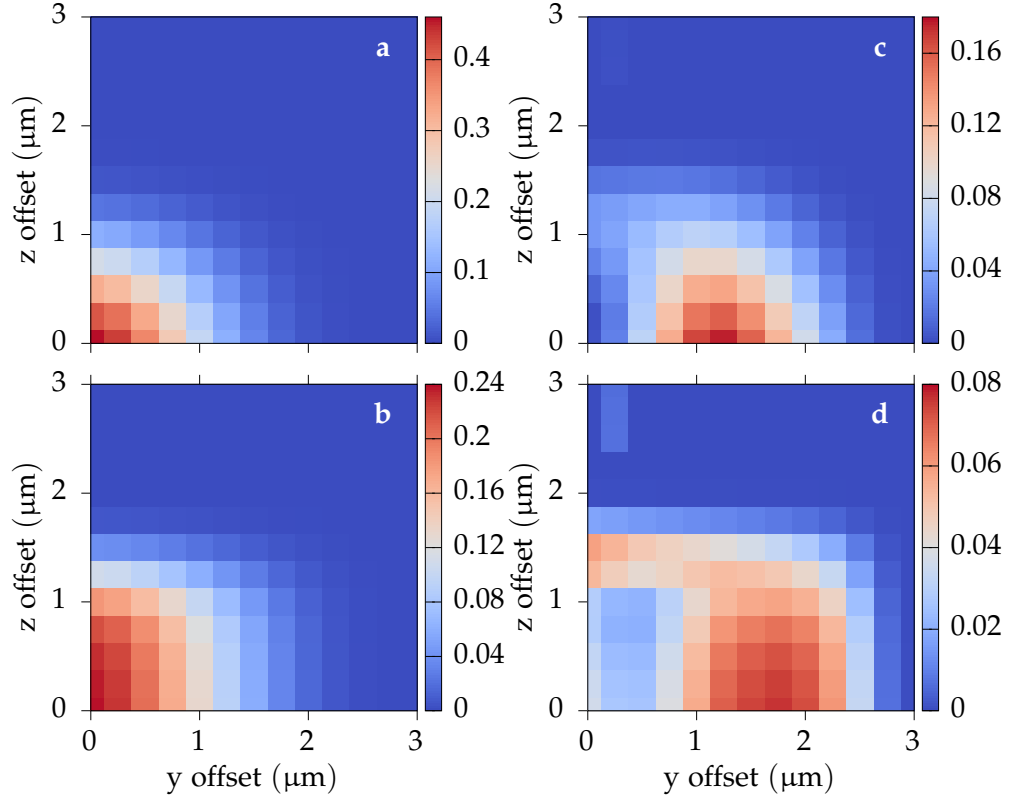


Figure 5.3: An incoming gaussian mode ($w_{waist} = 1.5\mu\text{m}$) couples with high efficiency with the fundamental modes if it is aligned with the core facet. If there is an offset along y or z , it couples more with the higher order modes. The coupling efficiency of a $NA = 0.5$ lens for fundamental modes (a) and all higher order modes (b) is compared with the coupling efficiency of a microlens optical fibre of $NA = 0.123$ for fundamental modes (c) and all higher order modes (d).

at $x_{offset} = 3\mu\text{m}$ from the waveguide facet couples with the fundamental modes with an efficiency of 435%, which is slightly below the 45% obtained as it is focused perfectly on the waveguide input facet. For the microlens optical fiber case, which presents a much smaller NA , the offset of the focal plane does not change the power coupling, which stays constant at 12%. Finally, we confirmed that the incoming beam must be linearly polarized at about 45° , specifically at: $\alpha = \text{atan}(\frac{\eta_{TM}}{\eta_{TE}}) = \text{atan}(\frac{0.2249}{0.2316}) = 44.16^\circ$.

5.2 Monomode Condition

The input coupling assures the waveguide to be almost monomode at the input section. According to fig. 5.3, in the piezo alignment window $\approx 40\%$ of the incoming beam power couples in the fundamental modes, while only $\approx 5\%$ couples in the other higher order modes. Still, in ideal monomode condition higher order modes should not be excited at all. So we add a bottle neck section to filter them completely. The reason is that the refractive index of the modes decreases as the confinement increases. Therefore they are less confined, in analogy to what would occur to the energy levels of trapped electrons in a quantum well. For sufficient small core width and height, the higher order modes leak into the high index *GaAs* substrates, as their effective index is smaller than the cladding: $n_{eff} < n_{cladding}$.

On the other hand, if the core width and thickness are too small, even the fundamental modes leak into the substrate, thus no modes can propagate in the waveguide.

Therefore the single mode condition is satisfied if $w \in [w_{min}, w_{max}]$ for a given height or $h \in [h_{min}, h_{max}]$ for a given width.

Since the core refractive index can be set within the range $n \in [2.98, 3.37]$, the exploration of the whole space of parameters (h, w, n) requires a high number of simulations. Eigenmodes or FDTD are not suitable for this task, since their calculation accuracy comes at the price of longer simulation time. To obtain a fast and complete overview of the space parameter, we implement in a matlab program an approximating method to quickly find the mode effective index, name Effective Index Method (EIM). In EIM one two-dimensional field problem $E(y, z)$ is simplified into two separate one-dimensional problems, $E(y)$ and $E(z)$. In our case, the 2D wire waveguide is approximated in two 1D slab waveguides, as fig. 5.4 illustrates.

The advantage arises from the fact that the effective index n_{eff} of the modes in an asymmetric slab waveguide can be calculated quickly via the analytical formula (eq. 5.2):

$$\tan(ht) = \frac{p + q}{h \left(1 - \frac{pq}{h^2}\right)} \quad (5.2)$$

where t is the slab thickness and h, p, q depends on the material refractive index:

$$h = \left[\left(\frac{n_2 w}{c} \right)^2 - \beta^2 \right]^{\frac{1}{2}}; \quad q = \left[\beta^2 - \left(\frac{n_1 w}{c} \right)^2 \right]^{\frac{1}{2}}; \quad p = \left[\beta^2 - \left(\frac{n_3 w}{c} \right)^2 \right]^{\frac{1}{2}} \quad (5.3)$$

In the first EIM step, the core is approximated by a slab waveguide, which has $w = w_{core}$. The calculated effective index n_{eff}^{1D} is used as refractive index of the slab in

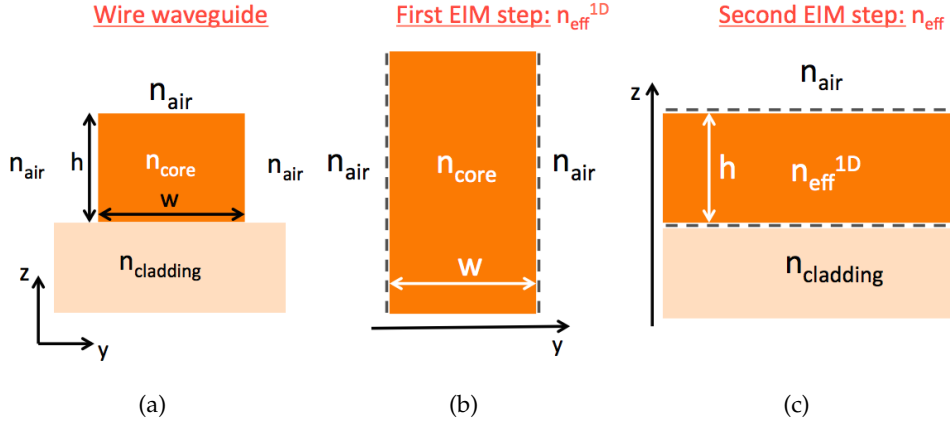


Figure 5.4: EIM method approximation principle: a 2D Wire waveguide (a) is decomposed in two 1D slab waveguides along y (b) and z (c). In (c) the core refractive index is given by the effective index of the mode calculated in the step (b).

the second EIM step, which approximates the wire waveguide along z , given the slab height $h = h_{core}$. In particular, for symmetry reason the quasi-TE n_{eff}^{1D} is used to calculate n_{eff} of the quasi-TM at the second step and viceversa.

To check the EIM approximation validity, we compare some of the calculated n_{eff} with the n_{eff} resulting from eigenmode simulation of the same waveguide.

An accuracy in the order of $\Delta n_{eff} = n_{eff}^{EIM} - n_{eff}^{eigenmode} \approx 10^{-3}$ is found out, so the method is reliable.

By launching the EIM script in a loop over the core thickness and width, we find the monomode map in the (w, h) space, presented in fig. 5.5. The monomode map is mostly situated at the bottom left part of the plot, as the monomode condition is satisfied for either sufficiently small core width or height. Only for $w \in [0.5\mu, 1.7\mu]$ the waveguide is monomode, so EBL is necessary for the patterning process. The map is not perfectly symmetric because in the vertical direction the core interfaces with a cladding $n_{clad} = 2.98$ on the bottom side, while along the horizontal direction is surrounded by air on both sides.

5.3 Delay

Given the (w, h) monomode condition map, we also investigate the delay between the quasi-TE and quasi-TM mode in function of (w, h) : $\Delta n(w, h) = n_{quasi-TE}(w, h) - n_{quasi-TM}(w, h)$. We confirm that it is possible to use an asymmetric waveguide to induce the delay, since $|\Delta n| \geq 0.1$, is obtained for a core either short and large or tall and narrow. The reason is that the effective index of a mode $n(w, h)$ changes abruptly near the cut-off condition. Quasi-TE cut-off condition depends mostly on the core width (w), while quasi-TM cut-off condition on the height (h), given their orthogonal polarization.

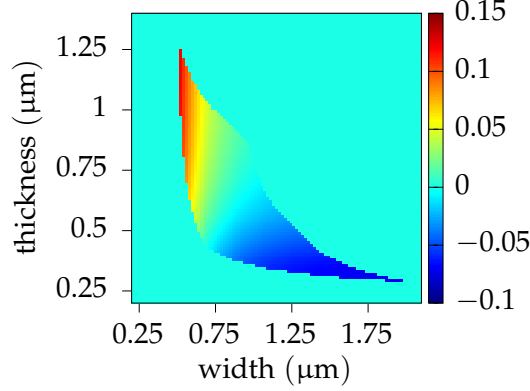


Figure 5.5: Monomode map in function of core width and thickness. For (h, w) satisfying the monomode condition, the difference in effective index between quasi-TE and quasi-TM mode is indicated. Otherwise, in zero mode or multi mode condition, a zero delay is returned.

Thus $|\Delta n(w, h)|$ is high when $\frac{w}{h}$ is very high or very low as compared to 1.

To choose the core height, we consider that it must be constant across the waveguide, as we aim for an easy fabrication process with only one etching step.

Thus small core thicknesses like $h_{core} = 0.4\mu\text{m}$ are not suitable as they do not allow an efficient input coupling and tolerable diffraction angle for the squared core at the output facet.

On the other hand, the core lateral dimension w , set by the electron beam, can be varied arbitrarily along the waveguide, within the EBL tolerances.

To obtain a non negligible delay, the core width is set to $w_2 = 0.55\mu\text{m}$ in the delay section, while the core height to $h = 1.08\mu\text{m}$. As. fig. 5.5 indicates, at (w_2, h) the refractive index between the quasi-TE and quasi-TM modes is $\Delta n \geq 0.1011$.

According to $\phi = k_0 \Delta n L_{delay}$, the delay section is $L_{delay} = 38.366\mu\text{m}$ long to obtain the desired $\frac{\pi}{2}$ phase-shift.

Since we operate close to the quasi-TE cut-off condition (for $w < 0.50\mu\text{m}$ the quasi-TE mode is not guided), a fabrication tolerance smaller than $\Delta w_{core} = 50\text{nm}$ is required, which is compatible with EBL.

EBL is slower than FB MS EBL, used to pattern the rest of the device, but $L_{delay} = 38.366\mu\text{m}$ is short enough to allow a fast fabrication process.

Finally, we remind that a well-defined OAM requires an exact $\frac{\pi}{2}$ phase-delay. So we verify that no additional phase-shift is inducted in the input and output sections of the waveguide.

The output section has a squared core ($w = h = 1.08\mu\text{m}$), so the two orthogonally polarized modes propagate with the same speed. Regarding the input section, $w = 3\mu\text{m}$ wide to ease the coupling, the difference in refractive index is negligible: $\Delta n = n_{TE} - n_{TM} = 3.308 - 3.300 = 0.008$.

5.4 Losses

As the light beam propagates in the waveguide core, a small part of it may tunnel through the cladding layer and leaks into the substrate. In guided modes, the amplitude of the electric field decreases exponentially in the cladding along the vertical direction z [32]. Thus the leaking through the cladding decreases exponentially with the cladding thickness h_{clad} . However, h_{clad} cannot be too high, as the MBE growth does not allow layers higher than $\approx 5\mu\text{m}$. Therefore we investigate the losses of the least confined mode for $h_{clad} \leq 5\mu\text{m}$, in all the three sections of the device (fig. 5.6). The losses are calculated from the imaginary part of the mode effective index, derived by eigenmode simulations.

We see that $t_{cladding} \approx 3\mu\text{m}$ is sufficient to assure our device, less than 1cm long, to be ideally lossless, as losses are $\approx 0\text{dB/cm}$.

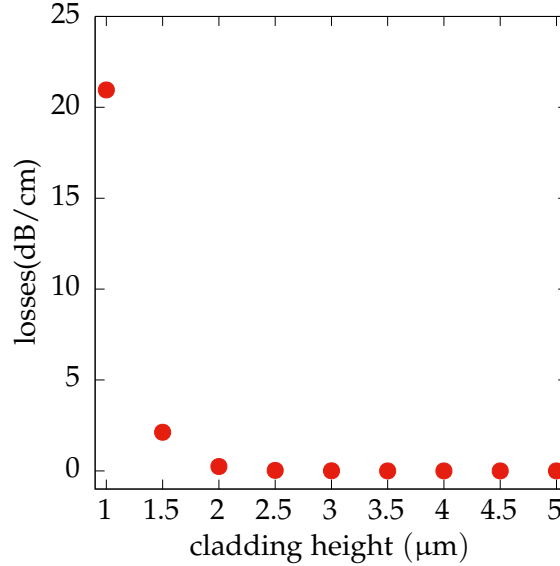


Figure 5.6: Propagation losses due to mode leaking into the substrate in input ($w_1 = 3\mu\text{m}$), delay ($w_{delay} = 0.55\mu\text{m}$) and output section ($w_o = 1.08\mu\text{m}$). $t_{cladding} \approx 3\mu\text{m}$ is sufficient to have an ideally lossless device.

In practice all the waveguides are affected by other sources of losses, given by imperfections due to fabrication. In *AlGaAs* the main source of losses is given by side-walls surface scattering. The core side walls, fabricated via EBL, are rough in the $\approx 10\text{nm}$ range. Thus a small part of the light is unavoidably reflected back by these scattering centers.

5.5 Diffraction

The beam carrying OAM, coming out of the waveguide, must be collected and characterised. At the device output, the finite size of the core width makes the beam diffract as it goes into free space. Thus a lens with sufficiently high numerical aperture $NA = \sin(\theta)$ is required to collect all (or at least most) of the emitted light.

To know the necessary NA we simulate how the beam diffracts in free space via FDTD.

Fig. 5.7 illustrates in log scale the power of the diffracting field. The diffraction angle is $\theta \approx 35^\circ$. This value is consistent with the theoretical prediction of diffracting OAM beams in the case of $l = 1$ [27].

Besides, we can clearly see in fig. 5.7 (b) the optical vortex in the E_x component of the field, signature that the beam is carrying an OAM.

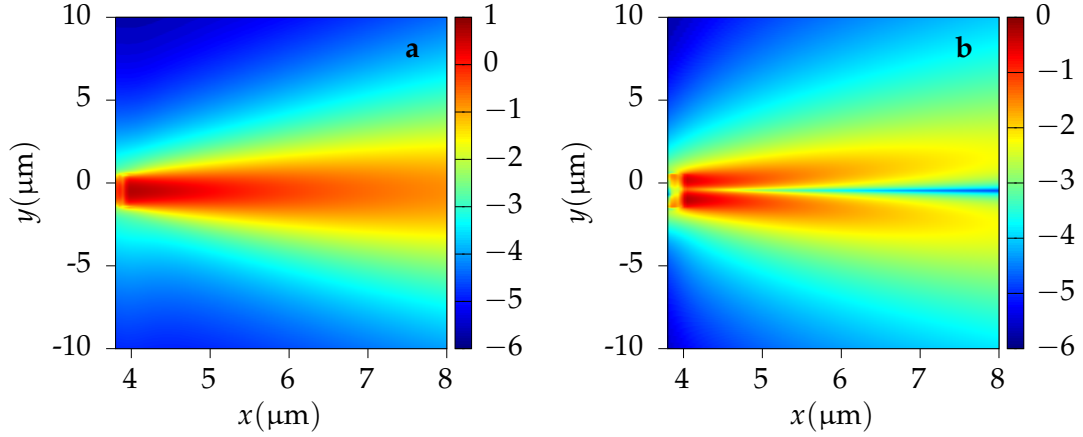


Figure 5.7: Top view of the generated SAM / OAM beam propagating in free space. Transversal P_t (a) and longitudinal P_x (b) field power components are compared (log scale).

5.6 Growth tolerances

The last tolerance to check concerns the growth process, after which $Al_xGa_{1-x}As$ layers present an uncertainty of $\Delta x = 5\%$ in the composition of Al . We verify that the found delay and monomode condition are not affected as x varies in $x \in [0.75, 0.85]$ and thus the refractive index in $n_{core} \in [2.95, 3.00]$ (plot 4.1).

The worst cases of $n_{core} = 2.95$ and $n_{core} = 3.00$ are presented in fig. 5.8. For the previously chosen geometry ($h = 1.08\mu m$, $w_{core} = 0.55\mu m$) the monomode condition is still satisfied. The delay is also unaffected, since $\Delta n_{n_{core}=3} = 0.1017 \approx \Delta n_{n_{core}=2.95} = 0.1013$.

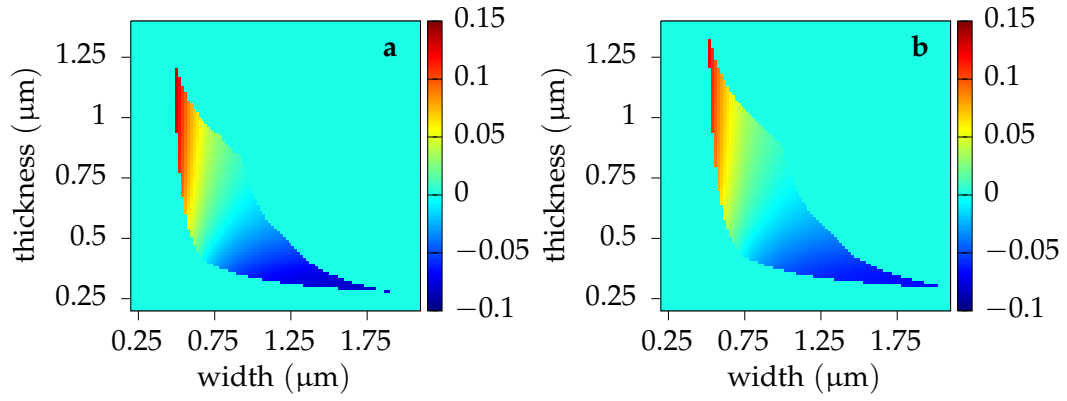


Figure 5.8: Evolution of the monomode and delay map in function of the core refractive index in order to predict the effect of errors in the growth. At $h = 1.08\mu m$ and $w_{core} = 0.55\mu m$, the monomode condition is always satisfied and the delay does not change, as we can see in the extreme case of $n_{core} = 2.95$ (a) and $n_{core} = 3.00$ (b).

6 Conclusion and Perspectives

In conclusion we have designed an AlGaAs on-chip device that converts a LP beam into a beam carrying OAM and SAM. Besides, the designed waveguide is ideally lossless, works in monomode condition and can be easily fabricated with EBL and FBMS EBL. Given its attractive features, we aim to fabricate it and characterize it in the next months.

As soon as the MBE growth is completed, we will proceed with the EBL/ FBMS lithography and etching. For this step we will design the EBL mask. Finally, we will proceed to its characterization. This part of the work will be carried on in partnership with the group of R. Boyd in Canada, specialized in quantum optics experiments using OAM. Getting the device working as designed, it will be the starting point for future on-chip quantum photonics circuits exploiting OAM.

For the next three years, I will continue this research at MPQ as a PhD student in the DON group, under the guidance of Sara Ducci. I would like to give my contribution to the generation, manipulation and detection of high dimensional Hilbert quantum states on AlGaAs integrated devices.

Bibliography

- [1] E. Abramochkin and V. Volostnikov. "Beam transformations and nontransformed beams." In: *Optics Communications* 83.1–2 (1991), pp. 123–135. ISSN: 0030-4018. DOI: [http://dx.doi.org/10.1016/0030-4018\(91\)90534-K](http://dx.doi.org/10.1016/0030-4018(91)90534-K).
- [2] Les Allen et al. "Orbital angular momentum of light and the transformation of Laguerre-Gaussian laser modes." In: *Physical Review A* 45.11 (1992), p. 8185.
- [3] Julio T. Barreiro. "Generation of Hyperentangled Photon Pairs." In: *Physical Review Letters* 95.26 (2005). DOI: 10.1103/PhysRevLett.95.260501.
- [4] V. Y. Bazhenov, M. S. Soskin, and M. V. Vasnetsov. "Screw Dislocations in Light Wavefronts." In: *Journal of Modern Optics* 39 (May 1992), pp. 985–990. DOI: 10.1080/09500349214551011.
- [5] V Yu Bazhenov, MV Vasnetsov, and MS Soskin. "Laser beams with screw dislocations in their wavefronts." In: *Jetp Lett* 52.8 (1990), pp. 429–431.
- [6] MW Beijersbergen et al. "Helical-wavefront laser beams produced with a spiral phaseplate." In: *Optics Communications* 112.5 (1994), pp. 321–327.
- [7] F. J. Belinfante. "On the current and the density of the electric charge, the energy, the linear momentum and the angular momentum of arbitrary fields." In: *Physica* 7 (May 1940), pp. 449–474. DOI: 10.1016/S0031-8914(40)90091-X.
- [8] Konstantin Y Bliokh, Aleksandr Y Bekshaev, and Franco Nori. "Dual electromagnetism: helicity, spin, momentum and angular momentum." In: *New Journal of Physics* 15.3 (2013), p. 033026.
- [9] J Courtial et al. "Rotational frequency shift of a light beam." In: *Physical review letters* 81.22 (1998), p. 4828.
- [10] C. G. Darwin. "Notes on the Theory of Radiation." English. In: *Proceedings of the Royal Society of London. Series A, Containing Papers of a Mathematical and Physical Character* 136.829 (1932), pages. ISSN: 09501207.
- [11] A. Padgett Franke-Arnold Sonja. "Advances in optical angular momentum." In: *Laser Photon. Rev.*, 2 (2008).
- [12] Sonja Franke-Arnold et al. "Uncertainty principle for angular position and angular momentum." In: *New Journal of Physics* 6.1 (2004), p. 103.
- [13] Severin Fürhapter et al. "Spiral phase contrast imaging in microscopy." In: *Optics Express* 13.3 (2005), pp. 689–694.
- [14] David J. Griffiths. *Introduction to Electrodynamics (3rd Edition)*. Benjamin Cummings, 1998. ISBN: 9780138053260.
- [15] NR Heckenberg et al. "Laser beams with phase singularities." In: *Optical and Quantum Electronics* 24.9 (1992), S951–S962.

- [16] Daniel F. V. James". "Measurement of qubits." In: *Physical Review A* 64.5 (2001). doi: 10.1103/PhysRevA.64.052312.
- [17] E. Karimi et al. "Efficient generation and sorting of orbital angular momentum eigenmodes of light by thermally tuned q-plates." In: *Applied Physics Letters* 94.23, 231124 (June 2009), p. 231124. doi: 10.1063/1.3154549. arXiv: 0905.0562 [physics.optics].
- [18] Johannes Kepler. *De Cometis Libelli Tres*. Avgvstae Vindelicorvm, A. Apergeri, 1619.
- [19] L. Lanco. "Semiconductor Waveguide Source of Counterpropagating Twin Photons." In: *Physical Review Letters* 97.17 (2006). doi: 10.1103/PhysRevLett.97.173901.
- [20] P. Lebedew. "Untersuchungen über die Druckkräfte des Lichtes." In: *Annalen der Physik* 311 (1901), pp. 433–458. doi: 10.1002/andp.19013111102.
- [21] Yao Liang et al. "Light beams with selective angular momentum generated by hybrid plasmonic waveguides." In: *Nanoscale* 6 (21 2014), pp. 12360–12365. doi: 10.1039/C4NR03606A.
- [22] R Loudon and C Baxter. "Contributions of John Henry Poynting to the understanding of radiation pressure." In: *Proceedings of the Royal Society of London A: Mathematical, Physical and Engineering Sciences*. Vol. 468. 2143. The Royal Society. 2012, pp. 1825–1838.
- [23] Alois Mair et al. "Entanglement of the orbital angular momentum states of photons." In: *Nature* 412.6844 (July 19, 2001), pp. 313–316.
- [24] L. Marrucci, C. Manzo, and D. Paparo. "Optical Spin-to-Orbital Angular Momentum Conversion in Inhomogeneous Anisotropic Media." In: *Physical Review Letters* 96.16, 163905 (Apr. 2006), p. 163905. doi: 10.1103/PhysRevLett.96.163905. arXiv: 0712.0099 [physics.optics].
- [25] SSR Oemrawsingh et al. "Production and characterization of spiral phase plates for optical wavelengths." In: *Applied optics* 43.3 (2004), pp. 688–694.
- [26] Adeline Orioux et al. "Efficient parametric generation of counterpropagating two-photon states." In: *J. Opt. Soc. Am. B* 28.1 (Jan. 2011), pp. 45–51. doi: 10.1364/JOSAB.28.000045.
- [27] Miles J Padgett et al. "Divergence of an orbital-angular-momentum-carrying beam upon propagation." In: *New Journal of Physics* 17.2 (2015), p. 023011.
- [28] MJ Padgett and J Courtial. "Poincaré-sphere equivalent for light beams containing orbital angular momentum." In: *Optics letters* 24.7 (1999), pp. 430–432.
- [29] Joseph Samuel and Rajendra Bhandari. "General setting for Berry's phase." In: *Physical Review Letters* 60.23 (1988), p. 2339.
- [30] J. W. Simmons and M. J. Guttman. *States, waves, and photons: A modern introduction to light*. 1970.
- [31] NB Simpson et al. "Mechanical equivalence of spin and orbital angular momentum of light: an optical spanner." In: *Optics letters* 22.1 (1997), pp. 52–54.
- [32] Allan W Snyder and J Love. *Optical waveguide theory*. Springer Science & Business Media, 2012.

- [33] Richard A. Soref, J. Schmidtchen, and K. Petermann. "Large single-mode rib waveguides in GeSi-Si and Si-on-SiO₂." In: *Quantum Electronics, IEEE Journal of* 27.8 (Aug. 1991), pp. 1971–1974. issn: 0018-9197. doi: 10.1109/3.83406.
- [34] M. S. Soskin et al. "Topological charge and angular momentum of light beams carrying optical vortices." In: *Phys. Rev. A* 56 (5 Nov. 1997), pp. 4064–4075. doi: 10.1103/PhysRevA.56.4064.
- [35] Keiichi Sueda et al. "Laguerre-Gaussian beam generated with a multilevel spiral phase plate for high intensity laser pulses." In: *Optics express* 12.15 (2004), pp. 3548–3553.
- [36] Fabrizio Tamburini et al. "Encoding many channels on the same frequency through radio vorticity: first experimental test." In: *New Journal of Physics* 14.3 (2012), p. 033001.
- [37] Fabrizio Tamburini et al. "Twisting of light around rotating black holes." In: *Nature Physics* 7.3 (2011), pp. 195–197.
- [38] GA Turnbull et al. "The generation of free-space Laguerre-Gaussian modes at millimetre-wave frequencies by use of a spiral phaseplate." In: *Optics communications* 127.4 (1996), pp. 183–188.
- [39] Jian Wang et al. "Terabit free-space data transmission employing orbital angular momentum multiplexing." In: *Nature Photonics* 6.7 (2012), pp. 488–496.
- [40] Frank Wilczek and Alfred Shapere. *Geometric phases in physics*. Vol. 5. World Scientific, 1989.
- [41] Alison M Yao and Miles J Padgett. "Orbital angular momentum: origins, behavior and applications." In: *Advances in Optics and Photonics* 3.2 (2011), pp. 161–204.